Sensitivity of Tropical Cyclone Intensity to Ventilation in an Axisymmetric Model

BRIAN TANG

National Center for Atmospheric Research, Boulder, Colorado*

KERRY EMANUEL

Massachusetts Institute of Technology, Cambridge, Massachusetts

(Manuscript received 8 September 2011, in final form 16 March 2012)

ABSTRACT

The sensitivity of tropical cyclone intensity to ventilation of cooler, drier air into the inner core is examined using an axisymmetric tropical cyclone model with parameterized ventilation. Sufficiently strong ventilation induces cooling of the upper-level warm core, a shift in the secondary circulation radially outward, and a decrease in the simulated intensity. Increasing the strength of the ventilation and placing the ventilation at middle to lower levels results in a greater decrease in the quasi-steady intensity, whereas upper-level ventilation has little effect on the intensity. For strong ventilation, an oscillatory intensity regime materializes and is tied to transient convective bursts and strong downdrafts into the boundary layer.

The sensitivity of tropical cyclone intensity to ventilation can be viewed in the context of the mechanical efficiency of the inner core or a modified thermal wind relation. In the former, ventilation decreases the mechanical efficiency, as the generation of available potential energy is wasted by entropy mixing above the boundary layer. In the latter, ventilation weakens the eyewall entropy front, resulting in a decrease in the intensity by thermal wind arguments.

The experiments also support the existence of a threshold ventilation beyond which a tropical cyclone cannot be maintained. Downdrafts overwhelm surface fluxes, leading to a precipitous drop in intensity and a severe degradation of structure in such a scenario. For a given amount of ventilation below the threshold, there exists a minimum initial intensity necessary for intensification to the quasi-steady intensity.

1. Introduction

Tropical cyclones (TCs) are often approximated as axisymmetric phenomena to first order, but asymmetric features are undoubtedly a fundamental part of TC structure. Although there is good understanding of the types of waves a TC supports, there remains uncertainty how these waves interact with the vortex to affect the TC's mean intensity. This study seeks to better understand one particular thermodynamic interaction, namely the effect of entropy mixing between the TC eyewall and the near-environment by asymmetric motions.

A particular subset of waves, called vortex Rossby waves, make up much of the low-wavenumber power in the inner core of the TC, particularly along the sharp radial gradient of potential vorticity just outside the radius of maximum wind. Vortex Rossby waves are hypothesized to be excited by various mechanisms, such as the breakdown of a high potential vorticity ring (Schubert et al. 1999), asymmetric diabatic heating (Wang 2002), and environmental vertical wind shear (Reasor et al. 2000).

Environmental vertical wind shear excites two types of vortex Rossby waves: the quasi-mode and sheared vortex Rossby waves. The quasi-mode is a wavenumber-one discrete vortex Rossby wave mode describing the tilt and precession of the vortex (Reasor and Montgomery 2001; Schecter et al. 2002). The quasi-mode can then decay by projection onto sheared vortex Rossby waves (Reasor et al. 2004). Sheared vortex Rossby waves can also result from any flow or temperature perturbation, such as asymmetric distributed convection due to vertical wind shear (Corbosiero et al. 2006).

* The National Center for Atmospheric Research is supported by the National Science Foundation.

Corresponding author address: Brian Tang, National Center for Atmospheric Research, P.O. Box 3000, Boulder, CO 80307.
E-mail: btang@ucar.edu

DOI: 10.1175/JAS-D-11-0232.1

Azimuthal perturbations caused by vortex Rossby waves can extend well beyond the inner core. For instance, Riemer et al. (2010) found that the perturbations induced by the tilt of the inner core in their simulation of a vertically sheared TC reach outward 40–50 km from the center, and the perturbations induced by the tilt of the outer vortex reach outward 150–200 km. The dispersion characteristics of sheared vortex Rossby waves also allow them to influence the TC structure away from their radii of excitation out to their stagnation radius, or the radius at which the radial group velocity vanishes (Montgomery and Kallenbach 1997). The stagnation radius roughly falls at 3 times the radius of maximum wind.

Vortex Rossby waves, like their midlatitude counterparts, advect and mix tracers. Mixing in TCs has been studied by investigating the steady flow topology (Riemer and Montgomery 2011), time-dependent flow topology (Sapsis and Haller 2009; Rutherford et al. 2010a,b), and effective diffusivity diagnostics (Hendricks and Schubert 2009). The time-dependent studies have found that vortex Rossby waves (and other transients) perform mixing that cannot be accomplished by the time-mean flow since strong vortices constitute a barrier to lateral mixing (McIntyre 1989). Two important quantities are mixed by eddies: momentum and entropy.

This study will focus on the effect of entropy mixing on TCs, but eddy momentum fluxes and their effect on the TC mean flow are also important. Eddy momentum–mean flow interactions have been studied in idealized models of TCs. Montgomery and Kallenbach (1997) first hypothesized that axisymmetrization of sheared vortex Rossby waves accelerates the mean tangential winds of the TC. This hypothesis is supported in both barotropic and baroclinic models for initially prescribed positive potential vorticity perturbations near the radius of maximum wind (Möller and Montgomery 1999, 2000). Eliassen–Palm flux diagnostics for a strengthening TC also show that eddy momentum fluxes accelerate and contract the maximum tangential winds in the lower troposphere (Chen et al. 2003). On the contrary, growing discrete vortex Rossby wave modes, such as induced by barotropic instability, weaken the intensity by extracting energy from the mean state (Kwon and Frank 2005). Additionally, Nolan and Grasso (2003) and Nolan et al. (2007) found that the perturbations induced by asymmetric heating weaken the TC due to downgradient eddy momentum fluxes and, instead, the symmetric response to the azimuthally averaged heating is much larger and responsible for the intensification.

In addition to eddy momentum fluxes, eddies affect the entropy distribution and budget of the inner core through ventilation. Ventilation is the flux of low-entropy environmental air into the TC's inner core (Simpson and Riehl 1958). Sufficiently strong vertical shear, or more precisely relative flow, can ventilate the TC by deforming the flow topology, allowing a pathway for environmental air to spiral in (Riemer and Montgomery 2011). However, the environmental air will not be able to intrude into the inner core unless the relative flow is sufficiently strong or the vortex is weak. Instead, flow perturbations induced by the quasi-mode and sheared vortex Rossby waves are one possible intermediary that can advect and mix low-entropy environmental air further inward.

Eddy entropy fluxes into the inner core are important to consider because low-entropy air frustrates the TC heat engine and constrains the intensity. Tang and Emanuel (2010, hereafter TE10) used an axisymmetric, steady-state, and slantwise neutral framework to show that ventilation acts to decrease the mechanical energy generation available to drive the TC's winds. The main findings from the idealized framework are 1) increasing ventilation nonlinearly reduces the steady-state intensity below the potential intensity; 2) ventilation acts to increase the initial intensity needed for a TC to intensify; and 3) there is a ventilation threshold beyond which only weakening TCs are possible. Additionally, ventilation acts to increase the outflow temperature or, equivalently, decrease the thermodynamic efficiency.

A handful of 3D moist numerical simulations have looked at ventilation in vertically sheared TCs, but the studies vary with the proposed ''flavor'' of the ventilation pathway. The first flavor is the upper-level pathway. Frank and Ritchie (2001) and Kwon and Frank (2008) found that vertical wind shear acts to excite asymmetries through both barotropic and baroclinic processes in the upper part of the vortex. They hypothesized that the asymmetries descend with time, weakening the vortex from the top down. Weakening occurs as the upper-level warm core is eroded by eddy heat fluxes, resulting in a hydrostatic increase in central minimum pressure. The second flavor is the midlevel pathway. Lagrangian back trajectory analysis of a sheared TC reveals that the eyewall is ventilated by parcels originating at midlevels. The midlevel ventilation results in a reduction of the eyewall equivalent potential temperature by about 1 K (Cram et al. 2007). The third flavor is the low-level pathway. Riemer et al. (2010) and Riemer and Montgomery (2011) found that low-entropy environmental air undercuts the TC's convection in their simulations. Subsequently, downdrafts carry the low-entropy air down into the boundary layer where it is swept into the TC's inner core via the secondary circulation. Albeit, surface fluxes may modify the low-entropy air substantially by the time it reaches the eyewall (Powell 1990). It is unclear which pathways are most detrimental to the TC.

Eddy kinetic energy may be higher at upper levels, but the entropy gradient is weak and eddy motions may lie along isentropes. On the contrary, eddy kinetic energy may not be as large at midlevels, but the entropy gradient is much more pronounced.

To address this issue, we assess the sensitivity of TC intensity to the various ventilation flavors in an axisymmetric, nonhydrostatic, and finite volume TC model, which is described in section 2. After a control run is presented in section 3, a suite of experiments and intensity diagnostics are used to study the sensitivity of TC intensity to the amplitude and height of a fixed region of ventilation in section 4. Another suite of experiments with an adaptive region of ventilation that follows the eyewall is used to evaluate the main findings of TE10 in section 5. Conclusions follow in section 6.

2. Model description

The current model is developed with two principles in mind. First, the model is designed to be computationally simple and, thus, retains some features of the Rotunno and Emanuel (1987, hereafter RE87) model that have made it useful for studying axisymmetric TC processes. Second, since entropy and energy budgets are powerful diagnostic tools for analyzing TCs, the model is designed such that mass, energy, and entropy are rigorously conserved in the absence of sources or sinks.

a. Governing equations

Like the RE87 model, the current model is phrased in cylindrical coordinates (r, ϕ, z) on an f plane and is nonhydrostatic, compressible, and axisymmetric. The prognostic variables chosen in this model are the radial, tangential, and vertical momentum per unit volume ($U = \rho_d u$, $V = \rho_d v$, $W = \rho_d w$); the pseudoadiabatic entropy per unit volume ($S_p = \rho_d s_p$); and the densities of dry air, water vapor, and liquid water (ρ_d, $\rho_v = \rho_d q_v$, $\rho_l = \rho_d q_l$), where q_v is the water vapor mixing ratio and q_l is the liquid water mixing ratio. The governing equations for these variables in flux form are

$$\frac{\partial U}{\partial t} = -\nabla \cdot (\mathbf{u}U) + \rho_d\left[v\left(f + \frac{v}{r}\right) - c_{pd}\theta_v\frac{\partial \Pi}{\partial r}\right] + D_U, \tag{1}$$

$$\frac{\partial V}{\partial t} = -\nabla \cdot (\mathbf{u}V) + \rho_d\left[-u\left(f + \frac{v}{r}\right)\right] + D_V, \tag{2}$$

$$\frac{\partial W}{\partial t} = -\nabla \cdot (\mathbf{u}W) + \rho_d\left[-g(1 + q_l) - c_{pd}\theta_v\frac{\partial \Pi}{\partial z}\right] + D_W, \tag{3}$$

$$\frac{\partial S_p}{\partial t} = -\nabla \cdot (\mathbf{u}S_p) + \rho_d\left[\frac{c_{pd}}{\theta}(R + \mathcal{H})\right] + D_{S_p}, \tag{4}$$

$$\frac{\partial \rho_d}{\partial t} = -\nabla \cdot (\mathbf{u}\rho_d), \tag{5}$$

$$\frac{\partial \rho_v}{\partial t} = -\nabla \cdot (\mathbf{u}\rho_v) - \rho_d M_{q_l} + D_{\rho_v}, \tag{6}$$

$$\frac{\partial \rho_l}{\partial t} = -\nabla \cdot (\mathbf{u}\rho_l) - \frac{\partial}{\partial z}(v_T\rho_l) + \rho_d M_{q_l} + D_{\rho_l}. \tag{7}$$

The remaining variables are the Coriolis parameter f, gravitational acceleration g, specific heat of dry air at constant pressure c_{pd}, the Exner function Π, potential temperature θ, virtual potential temperature θ_v, and terminal velocity of raindrops v_T; D, R, $\mathcal{H}$, and M refer to turbulent, radiative, dissipative heating, and microphysics terms, respectively. Details of these terms can be found in the appendix.

The virtual potential temperature is defined as

$$\theta_v = \theta\frac{1 + (R_v/R_d)q_v}{1 + q_v}, \tag{8}$$

where R_v is the gas constant of water vapor and R_d is the gas constant of dry air. Additionally, the Exner function is now a diagnostic variable. Upon using the ideal gas law [$p = \rho_d(1 + q_v)R_d\theta_v\Pi$],

$$\Pi = \left(\frac{p}{p_b}\right)^{R_d/c_{pd}} = \left[\frac{R_d}{p_b}\rho_d(1 + q_v)\theta_v\right]^{R_d/c_{vd}}, \tag{9}$$

where p is the pressure, p_b is the base state pressure at the surface, and c_{vd} is the specific heat of dry air at constant volume.

Summing (5)–(7) yields a conservation equation for the total mass:

$$\frac{\partial \rho_t}{\partial t} = -\nabla \cdot (\mathbf{u}\rho_t) - \frac{\partial}{\partial z}(v_T\rho_l) + D_{\rho_v} + D_{\rho_l}, \tag{10}$$

where $\rho_t = \rho_d + \rho_v + \rho_l$ is the total density. The second term on the rhs of (10) reflects the effect of falling precipitation on the mass budget.

ENTROPY EQUATION

A number of cloud models have used moist entropy as a prognostic variable in order to take advantage of the fact that it is conserved for reversible moist adiabatic processes and absolves one from having to explicitly compute diabatic heating due to phase changes. For example, Ooyama (1990, 2001) proposed a dual state entropy formulation for moist numerical models

depending on the presence of condensate, and Zeng et al. (2005) developed a model with a comprehensive moist entropy equation to study the interaction between clouds and large-scale circulations.

Commonly, approximations are made to the full entropy or another adiabatic invariant in order to arrive at a more tractable expression and to save computational costs (Lipps and Hemler 1980; Tripoli and Cotton 1981; Bryan and Fritsch 2004). The assumption used in this model is to neglect the contribution of liquid water and ice entropy, also known as the pseudoadiabatic approximation.

The model's entropy equation, given by (4), is now derived. Upon ignoring the contribution of liquid water, the first law of thermodynamics for moist air can be expressed as

$$ds_p = (c_{pd} + q_v c_l) d \ln(T) + d\left(\frac{L_v q_v}{T}\right) - R_d d \ln(p_d) - R_v d(q_v \ln H), \quad (11)$$

where c_l is the specific heat of liquid water, L_v is the latent heat of vaporization, T is the temperature, p_d is the dry pressure, and H is the relative humidity (Emanuel 1994). Bryan (2008) noted that the $q_v c_l d \ln(T)$ term can be ignored for a wide range of atmospheric conditions by compensating it with a fixed, inflated value of $L_v = L_{vo}$. Following this approach and integrating (11) from a reference state—defined to be at a temperature of 1 K, a water vapor mixing ratio of 0 kg kg^{-1}, and a dry pressure of 1 Pa—to the saturation level results in

$$s_p = c_{pd} \ln(T_L) + \frac{L_{vo} q_{vL}}{T_L} - R_d \ln(p_{dL}), \quad (12)$$

where variables with subscript L are evaluated at the saturation level.

The final simplification to (12) is to substitute in an empirical relationship for T_L since a simple analytical formula for T_L does not exist. The saturation level temperature is a function of both θ and q_v but is most sensitive to q_v for the range of atmospheric conditions of interest, namely the mean tropics. To demonstrate this, Fig. 1 shows values of T_L as a function of q_v. Each set of symbols is for a different pair of temperatures and pressures from the Jordan mean hurricane season sounding (Jordan 1958) but with the relative humidity varying from 10% to 100%; T_L is calculated using the empirical formula from Bolton (1980):

$$T_L = \frac{2840}{3.5 \ln(T) - \ln(e/100) - 4.805} + 55, \quad (13)$$

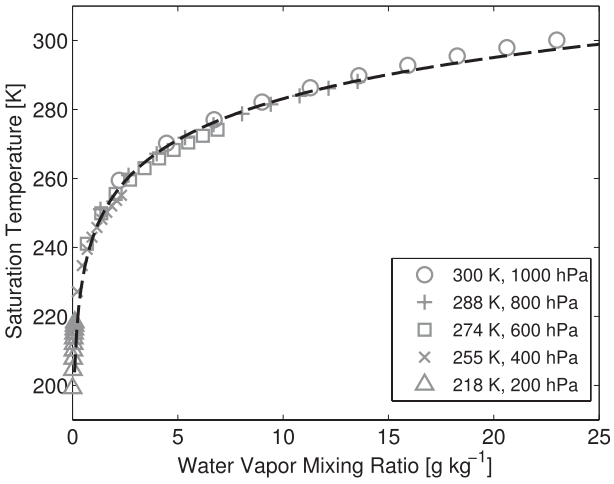

FIG. 1. The saturation temperature T_L as a function of the water vapor mixing ratio q_v, where each set of symbols is for a fixed combination of temperature and pressure with relative humidity varying between 10% and 100%. The empirical fit for T_L is given by the dashed line.

where e is the vapor pressure. To a reasonable degree, each set symbols overlaps with one another, indicating little sensitivity of T_L to combinations of mean temperature and pressure found in the tropics. Therefore, T_L can be approximated solely as a function of q_v. Applying a logarithmic fit to the data in a least squares sense results in the following empirical parameterization for T_L, which is defined as $\hat{T}_L$:

$$\hat{T}_L = \mathrm{MAX}[A \ln(q_v) + B, A], \quad (14)$$

where $A = 17.23$ and $B = 362.48$. The empirical curve representing $\hat{T}_L$ is plotted in Fig. 1 as the dashed black line. It will be clear later why $\hat{T}_L$ cannot be allowed to drop below A. Additionally, it should be emphasized that (14) is calibrated for a mean tropical environment and would need to be recalibrated for other purposes.

Using (14) and the definition of the potential temperature results in a simplified expression for s_p:

$$s_p = c_{pd} \ln(\theta) + \frac{L_{vo} q_v}{\hat{T}_L} - R_d \ln(p_b), \quad (15)$$

or, in terms of an pseudoequivalent potential temperature θ_{ep}:

$$\theta_{ep} = \theta \exp\left(\frac{L_{vo} q_v}{c_{pd} \hat{T}_L}\right), \quad (16)$$

such that $s_p = c_{pd} \ln(\theta_{ep}) - R_d \ln(p_b)$.

There is a clear advantage in expressing T_L only in terms of q_v, as it makes the second term on the rhs of (15) or the exponent in (16) only a function of q_v. This simple dependence on q_v allows for an equally simple conservation equation for s_p that can be derived by taking the total derivative of (15):

$$\frac{ds_p}{dt} = \frac{c_{pd}}{\theta}\frac{d\theta}{dt} + \frac{L_{vo}(\hat{T}_L - A)}{\hat{T}_L^2}\frac{dq_v}{dt}. \qquad (17)$$

Clearly, $\hat{T}_L$ cannot be allowed to be less than A, as this would correspond to a negative latent energy. For unsaturated adiabatic displacements, both θ and q_v are conserved, resulting in the desired property that s_p is also conserved. For saturated adiabatic displacements, condensation (evaporation) and latent heating (cooling) are constrained to conserve s_p.

The fixed value of the latent heat of vaporization is the remaining parameter that must be calibrated. Bryan (2008) and Davies-Jones (2009) both optimized approximations of s_p using inflated values of L_{vo} in order to minimize the error in s_p. A similar approach is taken here by comparing (16) with a highly accurate formula devised by Davies-Jones.[1] Similar to T_L, the optimization is performed for temperature profiles that are ±5 K around the Jordan mean hurricane season sounding along with the full range of relative humidity. Minimizing the rms error (RSME) over this phase space yields a value for L_{vo} of 2.678×10^6 J kg^{-1} with an RMSE of 0.24 K, comparable in accuracy to other approximations of θ_{ep}.

Using the optimized value of L_{vo}, the difference in temperature and water vapor mixing ratio profiles between two initially identical parcels (T = 28°C, H = 75%, and p = 1015 hPa) lifted using (17) and (11) is shown in Fig. 2. Errors are small below the lifting condensation level. Above the lifting condensation level, the parcel tends to be slightly too warm and moist. The temperature error is largest in the middle to upper troposphere, while the water vapor mixing ratio error is largest at midlevels.

b. Numerical methods

The prognostic variables are staggered using an Arakawa C grid (Arakawa and Lamb 1977) with a radial grid spacing of 2 km and vertical grid spacing of 300 m. Flux terms are calculated using a finite volume, corner-transport method with a monotonized central flux limiter (Durran 1999; LeVeque 2002), which has the desired quality of momentum, mass, and entropy conservation when there are neither fluxes at the boundaries of the computational domain nor internal sources. Time stepping is performed using an explicit third-order Runge–Kutta method with a split time step and an acoustic filter on the pressure terms, similar to that employed in the Weather Research and Forecasting Model (Wicker and Skamarock 2002; Klemp et al. 2007). Reflection of gravity waves at the outer boundary (r = 1000 km) is prevented by specifying an "outflow" boundary condition, following Klemp and Wilhelmson (1978) and RE87. Below the top of the domain (z = 24 km), a sponge layer with a thickness of approximately 5 km is used with implicit Rayleigh damping (Klemp et al. 2008).

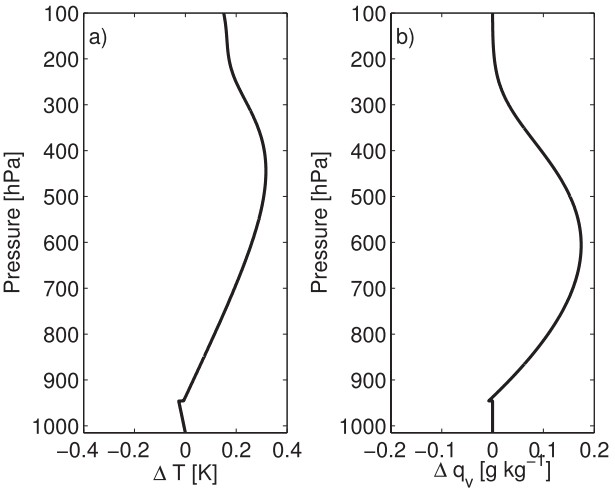

FIG. 2. The difference in (a) temperature and (b) water vapor mixing ratio between two initially identical parcels lifted pseudoadiabatically using the current formulation (17) and the full formulation (11).

3. Initialization and spinup

The model is initialized with a sounding, shown in Fig. 3, that is neutral to undilute ascent of subcloud layer parcels. In this study, the sounding is derived from a surface parcel with an initial pressure of 1015 mb, an initial temperature equal to a sea surface temperature of 28°C, and an initial relative humidity of 75%. The parcel is lifted such that it conserves s_p. To have a tropopause and stratosphere, the Jordan mean hurricane season temperature profile is used above the height where the lifted parcel first becomes cooler than the Jordan sounding. The water vapor mixing ratio below the parcel's lifting condensation level is retained. Above the lifting condensation level, the relative humidity is set at 50% so that evaporation and downdrafts can occur.

[1] See (6.5) in Davies-Jones (2009) for a θ_{ep} formula that is accurate to within 0.095 K for wet-bulb potential temperatures less than 40°C.

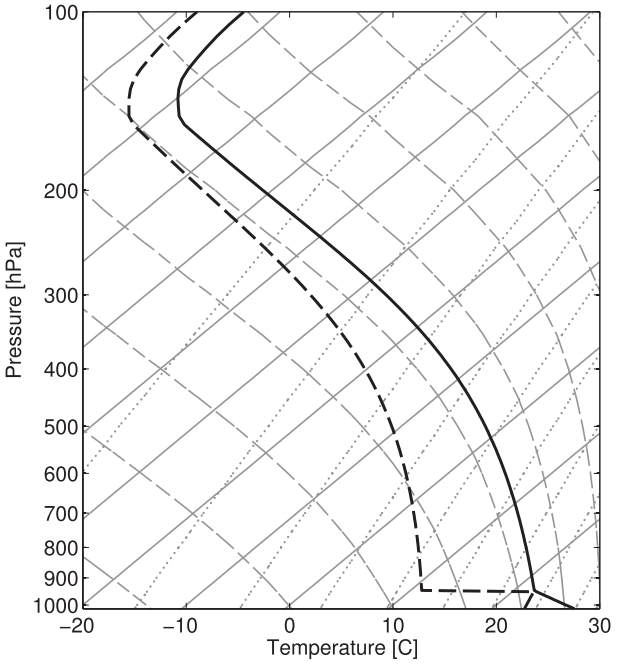

FIG. 3. The initial model neutral sounding plotted on a skew T–log$p$ diagram. The temperature profile is given by the thick black line and the dewpoint profile is given by the dashed black line. Water vapor mixing ratio isopleths (dotted lines) and pseudoadiabats (dashed gray lines) are also shown.

A tropical-storm-strength vortex is inserted in to the domain with the Coriolis parameter set to 5×10^{-5} s^{-1}. The vortex has a maximum tangential wind speed of 20 m s^{-1} at a radius of 100 km, and the radial profile of the tangential wind follows the parametric formula of Emanuel (2004) with an outer radius of 500 km. In the vertical, the tangential wind is maximum at the surface and vanishes at the tropopause. Additionally, the temperature and mass fields are adjusted to be in thermal wind balance with the initial vortex, following the anelastic approximation from Smith (2006).

The TC is spun up from its initial state until it reaches a steady state at seven days, as shown in Fig. 4. The maximum tangential winds are 67 m s^{-1} at a height of 1 km and a radius of 25 km. The radius of maximum wind slopes outward to 50 km at a height of 12 km. The secondary circulation, outlined by the mass streamfunction in Fig. 4a, consists of strong inflow in the lowest 1 km, deep slantwise rising motion in the eyewall over a radial annulus of approximately 20 km about the radius of maximum wind, and strong outflow around a height of 13–15 km. The waviness of the streamfunction as it rises up the eyewall is indicative of an inertial oscillation caused by unbalanced flow. A column of high, nearly constant entropy exists in the eyewall. Much lower values of entropy are found at midlevels outside the eyewall with the lowest values occurring at a height of 2–3 km. At this level relatively dry air from aloft has subsided and cooled radiatively. Elsewhere, there is shallow convection occurring outside the eyewall, but the stabilization caused by subsidence from the TC's thermally direct circulation and the resulting convective inhibition prevents the formation of deep convective rainbands.

4. Fixed ventilation experiments

A suite of experiments, listed in Table 1, is used to assess TC sensitivity to the ventilation strength and height. After the TC reaches a steady state, a ventilation

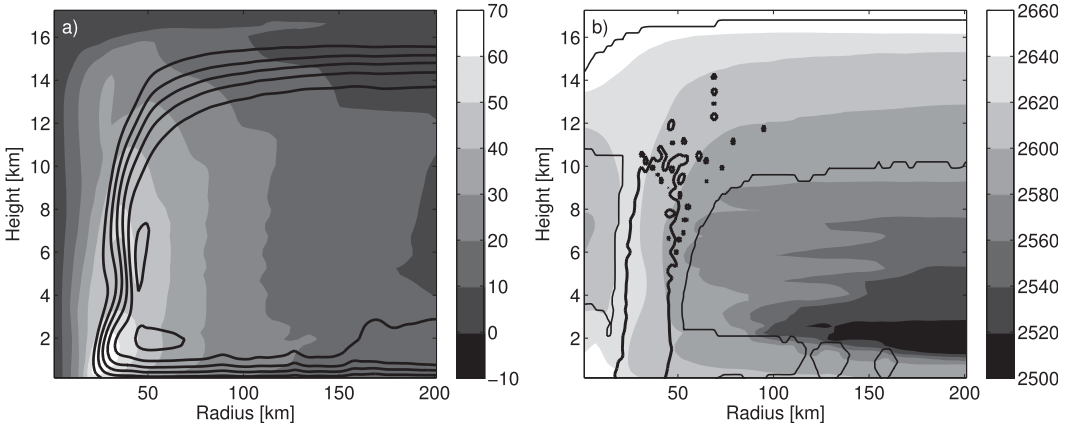

FIG. 4. Radius–height section of (a) the tangential velocity (shaded, m s^{-1}) and mass streamfunction (contoured, kg s^{-1}) and (b) the pseudoadiabatic entropy (shaded, J kg^{-1} K^{-1}) and liquid water mixing ratio (contoured) 7 days after initialization. For the liquid water mixing ratio, the thin contour is 0 g kg^{-1} and the thick contour is 1 g kg^{-1}, which is the threshold for rain. Only the inner 200 km and the lowest 17 km are shown.

TABLE 1. Fixed ventilation experiments. The columns from left to right give the experiment designation, the effective viscosity amplitude, and the radii and heights used in the localization function.

Expt	ν_e (m^2 s^{-1})	r_1 (km)	r_m (km)	r_2 (km)	z_1 (km)	z_2 (km)
Ctrl	0	NA	NA	NA	NA	NA
A01	1.0×10^4	20	30	60	2	4
A05	5.0×10^4	20	30	60	2	4
A10	1.0×10^5	20	30	60	2	4
A30	3.0×10^5	20	30	60	2	4
A50	5.0×10^5	20	30	60	2	4
H01	5.0×10^5	15	25	55	0	2
H03	5.0×10^5	20	30	60	2	4
H06	5.0×10^5	30	40	70	5	7
H09	5.0×10^5	35	45	75	8	10
H12	5.0×10^5	40	50	80	11	13
H15	5.0×10^5	40	50	80	14	16

region is introduced by adding a term to the turbulent entropy flux parameterization to reflect a fixed area of enhanced entropy mixing between the eyewall and near-environment:[2]

$$F_r^{s_p} = \cdots - \mathcal{L}(r,z)\rho_d \nu_e \frac{\partial s_p}{\partial r} \tag{18}$$

in which ν_e is a fixed effective eddy viscosity and

$$\mathcal{L}(r,z) = \begin{cases} (r - r_1)/(r_m - r_1) & \text{if } r_1 < r < r_m \text{ and } z_1 < z < z_2 \\ (r_2 - r)/(r_2 - r_m) & \text{if } r_m < r < r_2 \text{ and } z_1 < z < z_2 \\ 0 & \text{otherwise,} \end{cases} \tag{19}$$

where r_1, r_2, z_1, and z_2 are the prescribed bounds of the ventilation region and r_m is the radius of maximum wind. The localization function limits the areal extent of the ventilation and is chosen to be a piecewise linear function in radius. The localization function obtains a maximum value of unity at the initial radius of maximum wind, where the eddy kinetic energy is maximized (Wang 2002), and linearly decreases to zero at r_1 and r_2. The radial extent of the ventilation region reflects a prescribed annulus where vortex Rossby waves are able to mix entropy between the eyewall and near-environment within the vortex Rossby wave stagnation radius (Montgomery and Kallenbach 1997). While the width of the ventilation region is kept constant at 40 km across all experiments, r_1, r_m, and r_2 are shifted depending on the initial location of the radius of maximum wind in each experiment. In the vertical direction the localization function limits the mixing between z_1 and z_2. The radii and heights in $\mathcal{L}$ for each of the following experiments in this section are given in Table 1.

[2] It should be emphasized that the enhanced mixing is only performed on entropy, and not momentum, in order to isolate the effects of ventilation.

The effective eddy viscosity accounts for the ability of vortex Rossby waves to transport tracers finite distances before diffusive effects cause irreversible mixing. Thus, the effective eddy viscosity is typically larger than the conventional eddy viscosity of the subgrid-scale turbulence parameterization in the model. By simple scaling, the order of the effective viscosity can be estimated by multiplying an approximate eddy radial scale (10^4 m) times the difference in mean tangential velocity across the eddy (10 m s^{-1}). This yields effective eddy viscosity magnitudes $O(10^5)$ m^2 s^{-1}. As a comparison, Hendricks and Schubert (2009) found that breaking vortex Rossby waves are capable of mixing tracers across radial distances of 60–80 km, with effective eddy viscosities ranging between $O(10^3)$ and $O(10^4)$ m^2 s^{-1}. Collectively, the range of possible values for ν_e reflects a high degree of uncertainty, and a large range is sampled in the experiments.

a. Ventilation amplitude

In the first set of "A" ventilation experiments, the amplitude of the eddy viscosity is varied from 1.0×10^4 m^2 s^{-1} to 5.0×10^5 m^2 s^{-1}. The mixing occurs between a height of 2 and 4 km and is initially concentrated along the large radial entropy gradient of the eyewall outer edge. Subsequently, the TC undergoes substantial

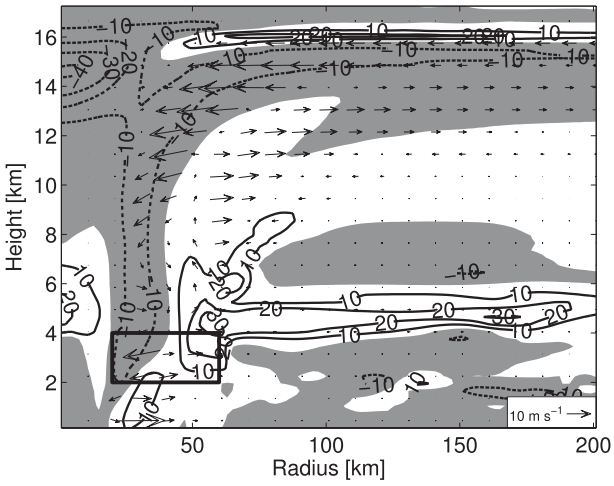

FIG. 5. Differences in entropy (contoured every 10 J kg^{-1} K^{-1}) and the secondary circulation (vectors, m s^{-1}) between the A50 and control experiments averaged over 24–48 h. Negative differences in entropy are shaded in gray. The rectangular box marks the ventilation region.

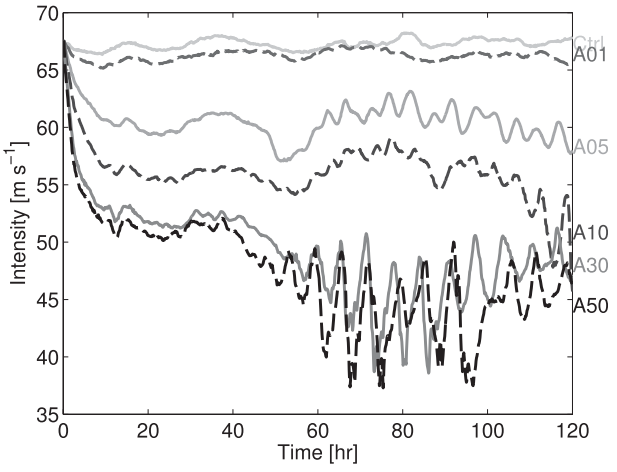

FIG. 6. The maximum tangential wind speed in the "A" ventilation experiments listed in Table 1.

intensity and structural changes if the ventilation is sufficiently strong.

Differences in the 24–48-h averaged entropy and secondary circulation fields between the experiment with the greatest mixing (A50) and the control experiment are shown in Fig. 5. The direct effect of the ventilation is to redistribute entropy within the bounds of the localization function, such that there is a decrease in entropy in the eyewall and an increase in the near-inner core region between a height of 2 and 4 km. Additionally, there are differences in entropy elsewhere including a decrease in entropy through a deep layer in the eyewall, an increase in entropy at midlevels out to 200 km due to convective detrainment, a large decrease in entropy in the eye at upper levels associated with a degradation of the upper-level warm core, and an increase in entropy in a thin strip at a height of 16 km associated with a warming of the convective cold top (Holloway and Neelin 2007). The vectors in Fig. 5 indicate differences in the secondary circulation of the TC between the A50 and control experiments. Ventilation has weakened the secondary circulation and shifted it radially outward and vertically downward aloft. The radius of maximum wind shifts radially outward from 25 to 40 km at a height of 1 km, and the eyewall mass flux is weaker because of the mixing of less buoyant parcels into the eyewall through the ventilation layer (not shown). Difference plots for the other experiments show similar patterns, albeit to a lesser degree. Hence, strong localized mixing over a small region across the eyewall induces systemwide changes in the thermodynamic and kinematic structures.

As may be inferred from the structural changes, there is a corresponding decrease in TC intensity to increasing ventilation amplitude, as shown in Fig. 6. For the A01 experiment, the weakening of the maximum tangential winds compared to the control run is barely discernible, whereas the TCs in the A30 and A50 experiments weaken approximately 15 m s^{-1} in the first 10 h. Thereafter, there are two starkly different intensity regimes: a quasi-steady regime and an oscillatory regime. All experiments are quasi-steady through 40 h. The A30 and A50 experiment then abruptly transition to a high frequency oscillatory regime where the intensity rapidly changes by 5–12 m s^{-1} over several hours. Furthermore, the mean intensity during the oscillatory period is lower than the intensity during the quasi-steady period.

Differences in the quasi-steady intensity can be explained by examining the mechanical efficiency η of the inner core. The mechanical efficiency is the ratio of the rate of work performed by the system divided by the rate of work that can be potentially achieved from the energy supplied to the system. In a steady state, the former can be measured by the integrated dissipation rate of mechanical energy. The latter is the generation rate of available potential energy, which comprises both surface entropy fluxes and dissipative heating (Pauluis and Held 2002). The mechanical efficiency is, therefore,

$$\eta = \frac{\int \mathcal{D}\rho_d \, dV}{\int (T - T_{\text{ref}})(F^{s_p}_{z=0} + \mathcal{D}/T)\rho_d \, dV}, \qquad (20)$$

where $\mathcal{D}$ is the dissipation rate, T_{ref} is the state-dependent reference temperature, and $F^{s_p}_{z=0}$ is the surface entropy flux. The reference temperature for each

point in the domain can be estimated by calculating each parcel's temperature at the level of neutral buoyancy in the sounding used to initialize the model. By construction, the initial sounding has zero available potential energy and is thus the model reference state.

Evaluating the terms in (20) over the entire domain of the control experiment reveals that the generation rate of available potential energy is much larger than the dissipation rate of mechanical energy. In a steady state this implies that another process must be siphoning the available potential energy away. The process responsible is the diffusion of entropy. In particular, the diffusion of entropy is represented by turbulent mixing and shallow convection outside the inner core acting to moisten and heat the environment. This results in a destruction of available potential energy, which otherwise could be converted to the vortex's mean kinetic energy. Hence, diffusion of entropy results in mechanical inefficiencies. Therefore, it is reasonable to expect that ventilation will cause a further reduction in mechanical efficiency as available potential energy is wasted to combat the intrusion of low-entropy environmental air into the inner core.

To diagnose the effects of ventilation on the mechanical efficiency, the integration domain of (20) is chosen to be the innermost 60 km and lowermost 17 km averaged over 24–48 h. This domain encompasses both the ventilation region and inner core. The mechanical efficiencies for the "A" ventilation experiments are shown in Fig. 7a. For increasing ventilation amplitude, the efficiency monotonically decreases from 75% in the control run to 57% in the A50 experiment.

The change in available potential energy due to ventilation can be quantified as the power loss due to entropy mixing. The power loss is equal to the integral of the product of the divergence of the entropy flux, including both the turbulence and ventilation parameterization terms, and the difference between the parcel temperature and reference temperature (Pauluis 2007):

$$\int (T - T_{\text{ref}}) D_{S_p} \, dV. \tag{21}$$

To see how entropy mixing results in a destruction of available potential energy, imagine two parcels with initially equal temperatures that exchange entropy. The first parcel is a saturated, eyewall parcel with high entropy and a reference temperature characteristic of the cold tropical tropopause. The second parcel is a dry, environmental parcel with low entropy and a reference temperature near its current temperature. Now, a small amount of entropy is fluxed from the eyewall parcel to the environmental parcel such that the reference temperatures do not change appreciably: D_{S_p} is equal and opposite for each parcel, with $D_{S_p} < 0$ for the eyewall parcel. However, since $(T - T_{\text{ref}})$ of the eyewall parcel is much larger than the environmental parcel, (21) is negative when summed over both parcels.

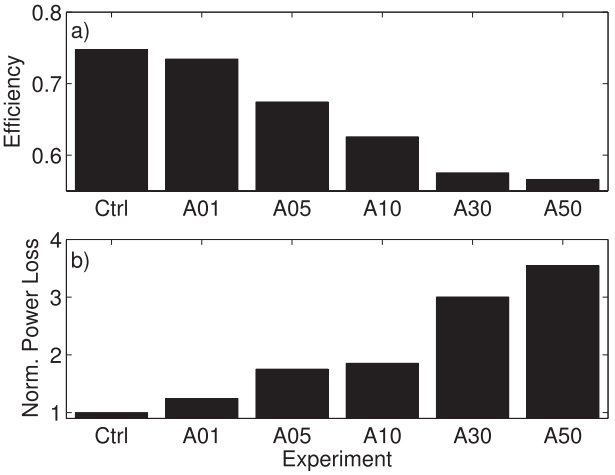

FIG. 7. (a) Mechanical efficiency for the "A" ventilation experiments and (b) the normalized power loss due to entropy mixing above a height of 2 km. The power loss is normalized by the control experiment value. Both quantities are calculated for the innermost 60 km and averaged over 24–48 h.

Figure 7b shows the power loss due to entropy mixing normalized by the control run's value over the same integration domain used to calculate the mechanical efficiency, excluding the lowest 2 km in order to prevent inclusion of surface fluxes. As the ventilation increases, the power loss increases significantly. For example, in the A50 experiment the power loss rises to 3.5 times that of the control experiment, or about 60% the magnitude of the power generated by surface fluxes in the same region. Thus, a large percentage of the available potential energy generation in the inner core is being destroyed by ventilation. This necessitates a lower mechanical efficiency and, subsequently, a lower intensity.

b. Ventilation height

In the second set of experiments, the ventilation height is varied from 0 to 16 km, while the effective viscosity is held at 5.0×10^5 m^2 s^{-1}. This set of experiments tests the weakening efficacy of ventilation at various heights by placing the localization function at different points along the outer edge of the eyewall. The TC intensity time series for these experiments are shown in Fig. 8.

Ventilation is most effective when it occurs at middle to low levels. Initially, the greatest weakening occurs for the H03 and H06 experiments with notably less weakening occurring as the ventilation layer is moved upward. The H01 experiment weakens less in the first 24 h compared to the H03 and H06 experiments, but continues

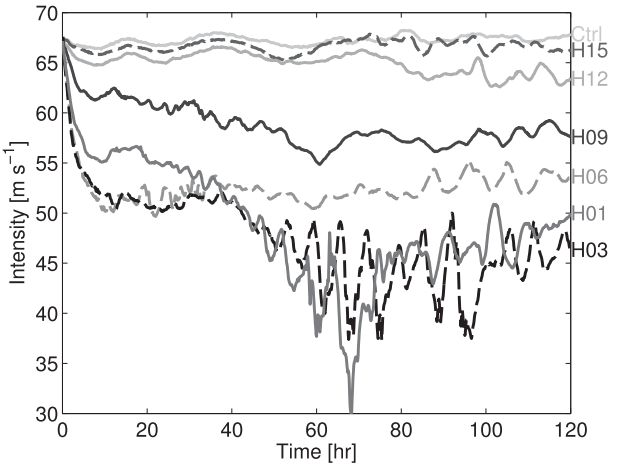

FIG. 8. The maximum tangential wind speed in the "H" ventilation experiments listed in Table 1.

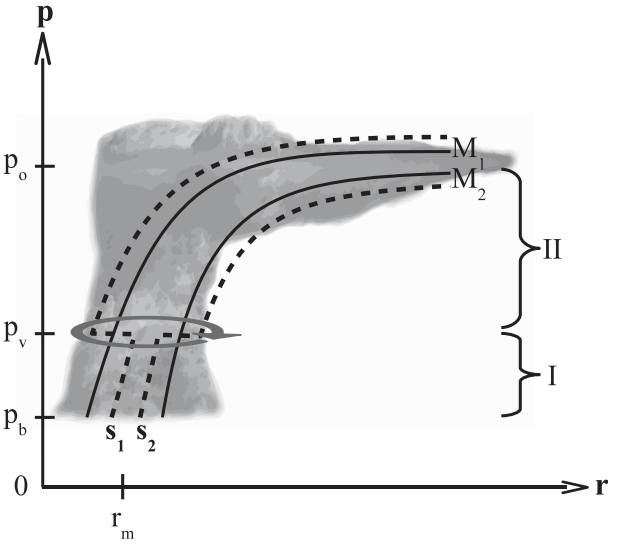

FIG. 9. Schematic of the simplified model that is used to derive the ventilation-modified thermal wind equation. The ventilation occurs at a single pressure level p_v. Region I, the layer below the ventilation, lies between the top of the boundary layer p_b and p_v. Region II, the layer above the ventilation, lies between p_v and the outflow layer p_o. Two angular momentum surfaces ($M_1 < M_2$) and two saturation entropy surfaces ($s_1 > s_2$) are shown, where there is a jump in the entropy gradient across the ventilation level.

to weaken and becomes approximately as weak as the H03 experiment after 40 h. In the H12 and H15 experiments, the TC intensity shows very little difference from the control run. Hence, ventilation above 11 km does not appear to be a mechanism that can substantially weaken a TC in this framework.

The degree to which ventilation affects the TC intensity in the "H" experiments is largely determined by the ability of eddy mixing to induce frontolysis in the eyewall entropy front. At midlevels this potential is maximized because a large low-entropy reservoir of relatively dry air exists in the near-inner core region that eddies can access (see Fig. 4b). At upper levels the radial gradient of entropy is very weak, reducing the ventilation potential. Thus, eddy kinetic energy can be very large at upper levels, but has little to no avail in thermodynamically inducing weakening. This is in contrast to the findings of Frank and Ritchie (2001), who hypothesized that a vertically sheared TC weakens due to ventilation at upper levels first.

Thermal wind balance provides a simple way of explaining how changing the ventilation height affects the quasi-steady intensity. Combining the expressions for hydrostatic balance and gradient wind balance by cross differentiating and using the definition of the angular momentum, $M = rv + 0.5fr^2$, the thermal wind relationship is

$$\frac{1}{r^3}\frac{\partial M^2}{\partial p}\bigg|_r = -\frac{\partial \alpha}{\partial r}\bigg|_p, \tag{22}$$

where α is the specific volume (Emanuel 1986). Since α can be expressed as a function of s_p^* and p, using the Maxwell relationship,

$$\frac{\partial T}{\partial p}\bigg|_{s_p^*} = \frac{\partial \alpha}{\partial s_p^*}\bigg|_p, \tag{23}$$

results in (22) becoming

$$\frac{2M}{r^3}\frac{\partial M}{\partial p}\bigg|_r = -\frac{\partial T}{\partial p}\bigg|_{s_p^*}\frac{\partial s_p^*}{\partial r}\bigg|_p. \tag{24}$$

Furthermore, since s_p^* is constrained to be a function of M at constant pressure,

$$\frac{2M}{r^3}\frac{\partial M}{\partial p}\bigg|_r = -\frac{\partial T}{\partial p}\bigg|_{s_p^*}\frac{\partial s_p^*}{\partial M}\bigg|_p\frac{\partial M}{\partial r}\bigg|_p. \tag{25}$$

Upon dividing (25) by $\partial M/\partial r$,

$$\frac{2M}{r^3}\frac{\partial r}{\partial p}\bigg|_M = \frac{\partial T}{\partial p}\bigg|_{s_p^*}\frac{\partial s_p^*}{\partial M}\bigg|_p. \tag{26}$$

An expression for the maximum tangential wind speed can be derived by integrating (26) down the angular momentum surface passing through the radius of maximum wind at the top of the boundary layer. To arrive at a simple expression, the two-layer system sketched in Fig. 9 is used. It is assumed that ventilation only occurs at a single pressure level p_v. Parcels rising through the eyewall

from region I to region II are instantaneously mixed as they cross the ventilation level, resulting in an instantaneous reduction in the magnitude of the entropy gradient across the eyewall. Additionally, it is assumed that neutrality holds above and below the ventilation level such that angular momentum and saturation entropy surfaces are congruent to one another in each separate region. As a result, the gradient of saturation entropy with respect to angular momentum can be expressed as

$$\frac{\partial s_p^*}{\partial M} = c_{\mathrm{I}} + \mathcal{F}(p_v - p)\underbrace{(c_{\mathrm{II}} - c_{\mathrm{I}})}_{\Delta c}, \tag{27}$$

where c_{I} and c_{II} are the (constant) entropy gradients across the eyewall in region I and region II and $\mathcal{F}(p_v - p)$ is the Heaviside step function centered at the ventilation level.

Under this set of assumptions, (26) can be integrated down the angular momentum surface passing through the radius of maximum wind in a piecewise manner:

$$M\left(-\frac{1}{r_m^2} + \frac{1}{r_o^2}\right) = \lim_{\delta \to 0} \int_{p_o}^{p_v - \delta} \left.\frac{\partial T}{\partial p}\right|_{s_p^*} (c_I + \Delta c)\, dp + \lim_{\delta \to 0} \int_{p_v + \delta}^{p_b} \left.\frac{\partial T}{\partial p}\right|_{s_p^*} c_I\, dp, \tag{28}$$

where r_o is the outer radius, p_o is the pressure of the outflow level, and p_b is the pressure at the top of the boundary layer. Upon evaluating the integrals and assuming $r_o \gg r_m$ and $T_{v-\delta} \approx T_{v+\delta}$,

$$-\frac{M}{r_m^2} = c_I(T_b - T_o) + \Delta c(T_v - T_o), \tag{29}$$

where T_b, T_v, and T_o are the temperatures at the top of the boundary layer, ventilation level, and outflow level, respectively. However, (29) does not take into account unbalanced effects that cause the tangential winds to be supergradient at the top of the boundary layer. Bryan and Rotunno (2009a) introduced a modification to potential intensity theory to account for unbalanced effects. Applying their modification and letting $M \approx rv$, (29) becomes

$$v_m^2 = -M_m[c_I(T_b - T_o) + \Delta c(T_v - T_o)] + r_m \zeta_m w_m, \tag{30}$$

where ζ is the azimuthal vorticity and w is the vertical velocity. Any variable with a subscript m is evaluated at the radius of maximum wind at the top of the boundary layer. The first term within brackets on the right-hand side is the classical expression from Emanuel (1986), where the maximum tangential wind speed is proportional to the constant entropy gradient in the eyewall. The second term within brackets represents a correction due to ventilation. Increasing Δc, that is, pulling entropy contours apart across the ventilation level, acts to decrease the magnitude of the term in brackets, resulting in a decrease in v_m. Increasing the temperature at which ventilation occurs weights the second term more and also results in a decrease in v_m. Finally, the final term on the right-hand side is the contribution of unbalanced effects.

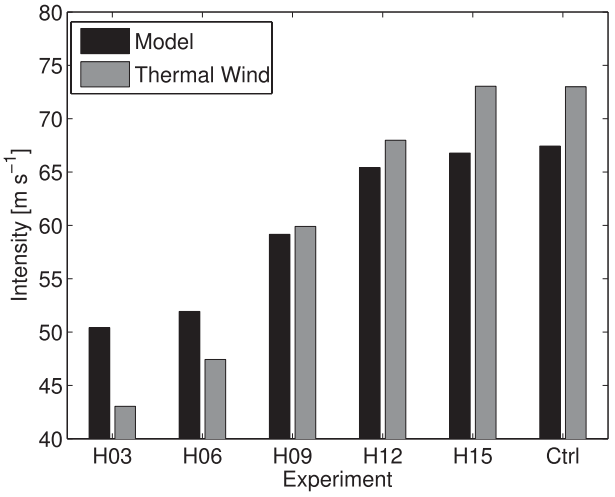

FIG. 10. The maximum tangential wind speed at a height of 1 km for the "H" experiments (black) and the theoretical maximum tangential wind speed using a modified thermal wind equation (30) in the eyewall (gray) averaged over 24–48 h.

The theoretical maximum tangential wind speed at a height of 1 km in the "H" ventilation experiments is calculated with (30) using the vertically averaged saturation entropy gradients along M_m above and below the ventilation layer.[3] Figure 10 shows the results of this calculation along with the model's maximum tangential wind speed at 1 km averaged over 24–48 h. The modified thermal wind equation does well at estimating the model's maximum tangential wind speed, with <10 m s^{-1} overestimation for the H12, H15, and control experiments and <10 m s^{-1} underestimation for the H03 and H06 experiments.

The behavior of the "H" experiments can be explained using the modified thermal wind relationship. Placing the

[3] In the H01 experiment, c_I is undefined since the ventilation layer extends to the surface.

ventilation at 3 or 6 km results in a large Δc as very low entropy air is mixed into the eyewall, resulting in a sharp jump in the entropy gradient across the ventilation layer. Moreover, $T_v - T_o$ is larger when the ventilation occurs lower in the eyewall, which increases the effect of the ventilation. The combination of these two effects results in a substantial decrease in the maximum tangential wind speed at the top of the boundary layer. As the storm weakens, a positive feedback results as c_I also decreases in magnitude due to weaker boundary layer inflow and surface fluxes both reducing the frontogenesis at lower levels. On the other hand, the background radial entropy gradient weakens when the ventilation is moved upward, resulting in less of a jump in the entropy gradient across the ventilation layer. This is especially true when the ventilation is placed above 10 km, which explains why the H12 and H15 experiments differ little from the control experiment. Additionally, as T_v approaches T_o, the second term in (30) vanishes and, thus, ventilation in the outflow layer has little bearing on the maximum tangential winds.

c. *Oscillatory intensity regime*

The quasi-steady intensity regime is described by the mechanical efficiency and thermal wind diagnostics fairly well since time tendencies in the entropy and energy budgets are negligible. Additionally, the eyewall remains predominately slantwise neutral. In contrast, the oscillatory regime of the A30 and A50 experiments is characterized by rapid shifts in the axisymmetric structure of the storm. Each oscillation in the intensity is governed by the life cycle of a convective burst. At first, strong mixing deposits high-entropy air into the near-inner-core environment resulting in potential slantwise instability (not shown). Subsequently, elevated slantwise convection erupts from a height of 3 km, and precipitation falling from the convective burst evaporates into the dry air below, inducing an intense downdraft of 2–3 m s^{-1}. The downdrafts transport a pocket of low-entropy air down into the boundary layer and induce compensating inflow through the middle troposphere, resulting in an additional inward flux of low-entropy environmental air. The low-entropy air in the boundary layer is then swept inward by the radial inflow, stabilizing the atmospheric column and causing convection to temporarily cease until surface fluxes restore the boundary layer entropy. The process repeats itself with a period of about 5–8 h. Similar behavior is noted in Riemer et al. (2010) in their 3D simulation of a vertically sheared TC, particularly the flushing of low-entropy air into the inflow layer and associated decreases in intensity (see their Fig. 13).

The life cycle of several of these convective bursts from the A50 experiment is shown in the Hovmöller plot in Fig. 11a. The gray shading is the entropy at the lowest model level ($z = 150$ m), while the white outlines denote significant downdraft entropy fluxes at a height of 1.5 km. Each downdraft transports a large amount low-entropy air into the boundary layer that is then advected inward. Surface fluxes act to restore the entropy, but not completely before the downdraft modified air reaches the radius of maximum wind ~30 km. The result is a decrease in the radial entropy gradient through a deep layer in the eyewall. In response, the intensity decreases sharply, as seen by the dips in tangential wind speed after each downdraft event in Fig. 11b. Only after these large downdraft events cease after 100 h does the TC begin to recover to a higher mean intensity.

5. Adaptive ventilation experiments

In the previous experiments, the ventilation is fixed in space by the localization function. However, the ventilation is not constant in time since it is a function of the entropy gradient, which evolves with time. In the following set of experiments, our goal is to compare the intensity of TCs with different but constant values of ventilation in time. Additionally, instead of specifying a fixed ventilation region, the ventilation adapts to the TC's state by moving with the location of the radius of maximum wind where the eddy kinetic energy is maximized.

To accomplish this, the maximum eddy entropy flux is specified to occur through the angular momentum surface, M_o 10 km radially outward from the radius of maximum wind from a height of 2–6 km. This angular momentum surface roughly demarcates the outer edge of the eyewall. The magnitude of the entropy flux at M_o is held constant between a value of 0–30 J K^{-1} s^{-1} m^{-2} and decreases linearly on either side such that it vanishes at the radius of maximum wind and at the outer boundary of the domain. Thus, low-entropy air radially outward from the eyewall is injected into the eyewall at a constant rate.

The ventilation λ is calculated using the following formula:

$$\lambda = \frac{1}{\rho_b \delta r (r_m + \delta r)} \int_{2\text{ km}}^{6\text{ km}} F_r^{s_p} r|_{M_o} \, dz, \tag{31}$$

where ρ_b is the density at the top of the boundary layer and δr is a characteristic width of the eyewall. The characteristic width of the eyewall is set to 20 km, which is the approximate width of the 1 m s^{-1} updraft region of the eyewall initially. Here λ can be interpreted as the eddy entropy flux through the outer edge of the eyewall normalized by the area of the eyewall annulus.

The experiments are run out 10 days, and Fig. 12 shows the final 12-h averaged maximum tangential winds as a function of λ. The experimental results can then be

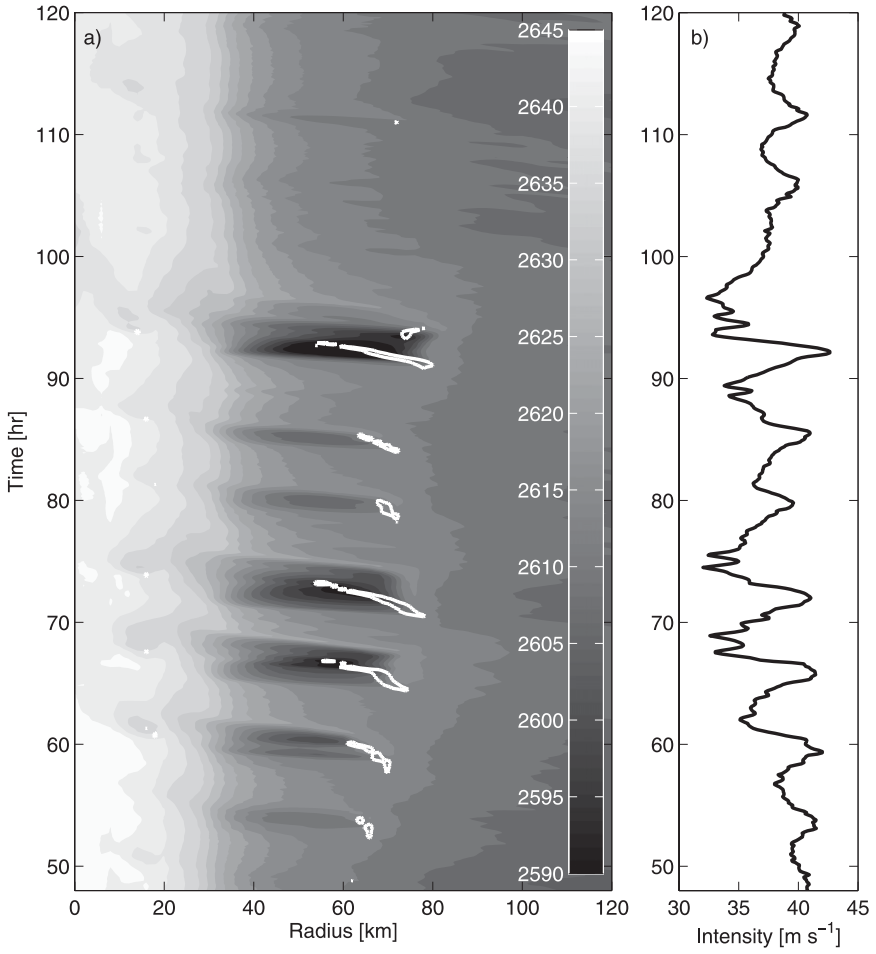

FIG. 11. (a) Hovmöller plot of the entropy at the lowest model level (shaded, J kg^{-1} K^{-1}) and significant downdraft entropy fluxes at 1.5 km (white outline at -3 m s^{-1} J kg^{-1} K^{-1}), and (b) the time series of maximum tangential wind speed (m s^{-1}) at the lowest model level from the A50 experiment.

compared with the theoretical steady-state intensity of a ventilated TC from TE10, given by the solution to

$$0 = v_m^3 - v_{\mathrm{PI}}^2 v_m + \frac{T_s(T_s - \overline{T_o})}{\overline{T_o}} \frac{1}{C_D} \lambda, \qquad (32)$$

where v_m is the maximum tangential wind speed, v_{PI} is the potential intensity, T_s is the surface temperature, and $\overline{T_o}$ is the mean outflow temperature. The appropriate potential intensity to use in this case is the model potential intensity, or the steady-state intensity of the control experiment. The real solutions of (32) are given by the solid and dashed gray lines in Fig. 12. The solid gray line is the only stable equilibrium and, thus, the only physically observable solution.

The first postulate from TE10 is that increasing ventilation causes a monotonic decrease in steady-state intensity. Clearly, this is also the case in the experiments.

The second postulate is that there exists a ventilation threshold beyond which only a weakening solution is possible. Based on model output, the ventilation threshold is estimated to be 4.7 m s^{-1} J kg^{-1} K^{-1}. The experiments that exceed the ventilation threshold have a precipitous drop in intensity, indicating that a threshold has been crossed. The experiments above the ventilation threshold are very disorganized with no well-defined radius of maximum wind and no coherent secondary circulation.

The precipitous drop in intensity can be attributed to downdrafts transporting overwhelming quantities of low-entropy air into the boundary layer, such that the generation of available mechanical energy by surface fluxes is unable to sustain the TC's winds against both dissipation and downdrafts. The downdraft entropy flux is defined as

$$\int \mathcal{F}(-W) W' s_p' r \, dr, \qquad (33)$$

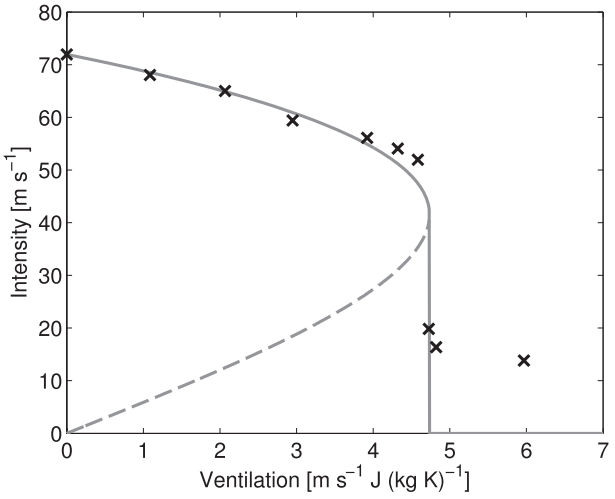

FIG. 12. The maximum tangential wind speed averaged over the final 12 h as a function of the ventilation for the adaptive ventilation experiments (crosses). The theoretical steady-state intensity from TE10 is given by the gray lines. The solid gray line denotes the stable equilibrium intensity, and the dashed gray line denotes the unstable equilibrium intensity.

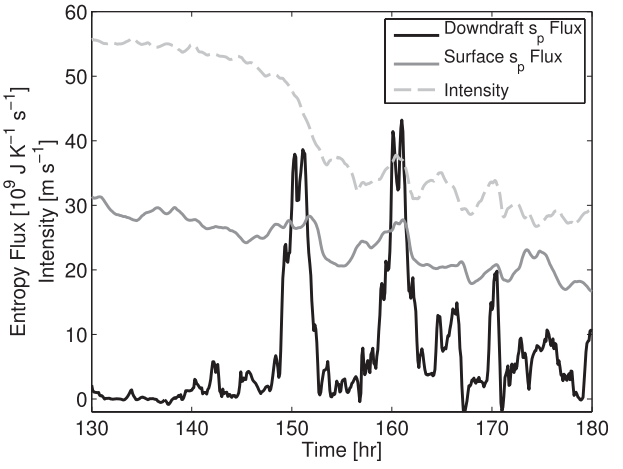

FIG. 13. The downdraft entropy flux at a height of 1.5 km (black line) and the surface entropy flux (gray line) integrated over an annulus between 20 and 60 km over a period of rapid weakening for the experiment with a ventilation of just under 5 m s^{-1} J kg^{-1} K^{-1}. Entropy fluxes are multiplied by 10^{-9}. The dashed light gray line is the maximum tangential wind speed.

where the Heaviside function $\mathcal{F}(-W)$ ensures that only downdrafts are included in the integrand. The primes refer to perturbations from a slowly varying mean, determined by running a low-pass filter through W and s_p at each point in the domain.

Figure 13 shows the integrated downdraft entropy flux at a height of 1.5 km and the integrated surface entropy flux for the experiment with a ventilation just under 5 m s^{-1} J kg^{-1} K^{-1}. Both quantities are evaluated over an annulus between 20 and 60 km. In the first 140 h, the downdraft entropy flux is small compared to the surface entropy flux, and the TC intensity only decays slowly from 67 to 55 m s^{-1}. However, the slow slide in intensity causes a concurrent decrease in surface entropy fluxes that makes the TC increasingly susceptible to the destructive effects of downdrafts. Starting at 148 h a very large downdraft event occurs. During this event, the downdraft entropy flux exceeds the surface entropy flux for a brief period of time. Note that there is a temporary increase in surface entropy fluxes despite the decrease in wind speed. This increase is a consequence of greater air–sea disequilibrium enhancing the surface fluxes, which mitigates the effects of downdrafts to a small degree. However, the degree of mitigation is not enough to prevent a precipitous drop in intensity. Another large downdraft event occurs around 160 h followed by a succession of moderate downdraft events with the greatest weakening lagging the downdraft events by a few hours. The elevated mean downdraft entropy flux thereafter, coupled with a significant drop in surface fluxes, causes the TC to continuously decay.

In the experiments where the ventilation exceeds the ventilation threshold, the TC does not weaken *rapidly* until the ventilation is communicated down to the boundary layer via strong downdrafts. There is some diffusion of entropy across the eyewall in the adaptive ventilation experiments but, since the ventilation is always radially outward of the radius of maximum wind, there is not nearly as much entropy mixing across the eyewall as in the fixed ventilation experiments. Therefore, an important finding arises concerning the ability of ventilation to weaken the TC. If ventilation is not communicated across the entire eyewall, as to affect the radial entropy gradient over a deep layer or communicated down to the boundary layer, where it can affect the energy budget in the TC's boundary layer, then ventilation only has a minor effect on the intensity in this framework.

The third postulate from TE10 is that there exists a minimum initial intensity required for strengthening for a given amount of ventilation. The theory predicts that TCs with initial intensities below the dashed line in Fig. 12 will decay, while TCs with initial intensities above it will strengthen to the steady-state intensity given by the solid line in Fig. 12. In this set of experiments, the ventilation is initiated at different times during the intensification stage of the control run. The ventilation is set to a value of 4 m s^{-1} J kg^{-1} K^{-1} for all experiments, which corresponds to a theoretical minimum intensity of 27 m s^{-1} required for strengthening after the onset of ventilation. Figure 14 shows the intensity time series from this suite of experiments. The storm with an initial intensity of 20 m s^{-1} fails to strengthen. For all other initial intensities, the TC strengthens and converges to approximately

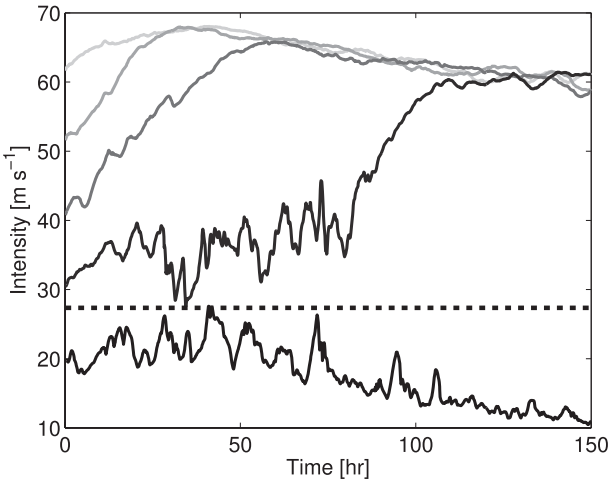

FIG. 14. The maximum tangential wind speed for the set of experiments in which the ventilation is initiated at different intensities. The dotted line is the lowest intensity required for intensification to the steady-state intensity, as calculated from the analytical solution of TE10 for the prescribed amount of ventilation.

the same intensity. Therefore, the results of this set of experiments supports the existence of a minimum intensity threshold between 20 and 30 m s^{-1} for the prescribed value of ventilation, consistent with the theory. However, since the intensity evolution has a stochastic component, it is possible that there exists a gray area around the theoretical minimum intensity threshold that contains both strengthening and weakening TCs.

6. Conclusions

Ventilation is hypothesized to constrain TC intensity through the flux of low-entropy environmental air into the TC inner core. A few flavors of the ventilation hypothesis include upper-level ventilation of the warm core (Frank and Ritchie 2001; Kwon and Frank 2008), midlevel ventilation of the eyewall (Simpson and Riehl 1958; Cram et al. 2007), and downdraft modification of the boundary layer due to the ventilation of near-inner core convection (Powell 1990; Riemer et al. 2010; Riemer and Montgomery 2011). An axisymmetric model is devised in order to assess the sensitivity of TC intensity to these possible ventilation pathways.

The model is based on the RE87 model, but has some notable differences and improvements. Some of these differences include a much more rigorously conserved budgets, the use of pseudoadiabatic entropy as a prognostic variable, and improved numerical methods.

Ventilation is parameterized in the model using a simple, downgradient diffusive flux of entropy that injects low-entropy environmental air into the eyewall over a prescribed region. A fixed region is used to study the sensitivity of TC intensity to ventilation amplitude and height, and an adaptive region based on the eyewall location is used to evaluate the findings of TE10.

Starting from a mature TC, ventilation is applied over a fixed area at midlevels across the eyewall with varying strength. In the experiments with strong ventilation, there is significant cooling of the upper-level warm core and a shift in the secondary circulation radially outward. Additionally, strong ventilation quickly weakens the TC, leading to a lower quasi-steady intensity. The reduction in intensity is the result of a lower mechanical efficiency due to entropy mixing above the boundary layer (Pauluis and Held 2002; Goody 2003). After a period of time, the simulations with strong ventilation transition in to an oscillatory regime characterized by rapid swings in the intensity of up to 12 m s^{-1} with a period of 5–8 h. These swings are shown to be associated with bursts of slantwise convection followed by a flux of low-entropy air down into the boundary layer by downdrafts. The cumulative effect of the downdrafts lowers the mean intensity further.

The sensitivity of the TC intensity to the ventilation height is also assessed by conducting experiments in which the ventilation is moved upward along the eyewall. The weakening decreases as the ventilation height increases. This behavior is explained using a modified thermal wind relationship. As the ventilation is moved upward, the change in the radial entropy gradient across the ventilation layer decreases in magnitude resulting in less of an effect on the tangential wind speed at the top of the boundary layer. Furthermore, as the temperature difference between the ventilation layer and the outflow layer decreases, ventilation becomes less effective at inducing weakening. The greatest weakening occurs when the ventilation occurs at middle to lower levels where the entropy difference between the eyewall and environment is greatest and the temperature difference between the ventilation layer and outflow layer is also relatively large.

Based on these findings, ventilation at midlevels appears to be an efficient mechanism by which a reduction in maximum intensity can occur. Additionally, downdraft modification of the boundary layer is also effective at reducing the efficiency of the hurricane heat engine and weakening the storm. However, upper-level ventilation does not appear to be an effective weakening mechanism in this framework.

In the adaptive ventilation experiments, the ventilation tracks with the eyewall location such that the eyewall is ventilated at a constant rate. These experiments allow key aspects of theoretical formulation from TE10 to be tested. Three components of the ventilation theory are supported: a monotonic reduction in intensity with

increasing ventilation; the presence of a ventilation threshold, beyond which a TC cannot exist; and a bifurcation of TC intensity based on the strength of the initial vortex.

Simply having the low-entropy air get close to the inner core has little effect in these experiments. To affect the energy budget of the TC and significantly weaken the storm, there must be substantial irreversible mixing of low-entropy environmental air with the high-entropy highway of the secondary circulation by either direct mixing across the entire eyewall or formation of downdrafts. Specifically with the latter, the TC rapidly weakens when the downdraft entropy flux becomes comparable to the surface entropy flux such that the mechanical energy generation by surface fluxes cannot maintain the TC winds against both dissipation and downdrafts.

The setup of the experiments is highly idealized, as the complicated details of how eddy entropy mixing actually occurs is not well understood. First, the ventilation parameterization does not reflect the possibility of nonlocal mixing, where entropy can be carried large distances before being irreversibly mixed at smaller scales. Second, there is large uncertainty in the appropriate values of the effective eddy viscosities. Estimates of effective eddy viscosities in a baroclinic vortex, particularly one under the influence of vertical wind shear, would be quite useful. Third, the region that is ventilated is not completely state dependent, whereas the dispersion characteristics of vortex Rossby waves depend strongly on the characteristics of the vortex (Montgomery and Kallenbach 1997), such as the radial gradient of potential vorticity. Finally, the handling of microphysics in this model is quite simplified, and the details of evaporation and melting of ice critically influence downdraft characteristics (Srivastava 1987). Thus, there is uncertainty as to how much of the results carry over to 3D simulations or nature. At the very least, the results from these idealized experiments show the need to evaluate the upper-level ventilation hypothesis more carefully and provide a basis for investigations of ventilation in more complex models.

The efficacy to which vertical shear-excited vortex Rossby waves are able to bring in low-entropy air into the inner core of the TC also needs to be studied in 3D models. A comprehensive analysis of the time-dependent flow topology or effective diffusivities of vertically sheared TCs would be elucidating.

Acknowledgments. We thank Mike Montgomery, John Molinari, Rich Rotunno, George Bryan, and three anonymous reviewers for their suggestions that helped improve an earlier version of this manuscript, which was one of the first author's dissertation chapters. This work was supported by NSF Grant ATM-0850639.

APPENDIX

Model Specifics

a. Microphysics

As done in the RE87 model, cloud water and rainwater are not considered separately. When $q_l \leq 1$ g kg^{-1}, all liquid water is in the form of cloud droplets with a terminal velocity of zero. On the other hand, when $q_l > 1$ g kg^{-1}, all liquid water is converted to rainwater and falls at a terminal velocity of -7 m s^{-1}. Although this is a drastic simplification, it eliminates a prognostic variable and the need to include a microphysics parameterization that converts cloud to rainwater and vice versa. Thus, all condensation and evaporation occurs at the grid scale. Derivation of the condensation algorithm follows that of Klemp and Wilhelmson (1978) with the new requirement that s_p, as defined in this model, be conserved.

The condensation/evaporation rate M_{q_l} is

$$M_{q_l} = \begin{cases} \dfrac{q_v - q_v^*}{\Delta t(1 + \chi q_v^*)} & \text{if} \quad H > 1 \\ \dfrac{1}{\Delta t}\text{MAX}\left[\dfrac{q_v - q_v^*}{(1 + \chi q_v^*)}, \; -q_l\right] & \text{if} \quad H < 1 \quad \text{and} \quad 0 < q_l \leq 1 \times 10^{-3} \\ \dfrac{1}{\hat{\tau}_{\text{evap}}}\text{MAX}\left[\dfrac{q_v - q_v^*}{(1 + \chi q_v^*)}, \; -q_l\right] & \text{if} \quad H < 1 \quad \text{and} \quad q_l > 1 \times 10^{-3}, \end{cases} \tag{A1}$$

where q_v^* is the saturation water vapor mixing ratio, Δt is the model time step, H is the relative humidity, $\hat{\tau}_{\text{evap}}$ is an evaporation limiter (explained below), and χ is defined as

$$\chi = \frac{4302.645\theta\Pi L_{vo}(\hat{T}_L - A)}{c_{pd}\hat{T}_L^2(\theta\Pi - 29.65)^2}. \tag{A2}$$

The constants in (A2) arise from using the Bolton (1980) formulation for the saturation vapor pressure. In the RE87 model, evaporation is assumed to occur just as rapidly as condensation and is limited only by the amount of liquid water present; that is, the relative humidity is constrained to be 100% in the presence of liquid water. While this assumption is good for cloud droplets, it overestimates the rate of evaporation of raindrops falling through unsaturated air, which can have an evaporation time scale on the order of tens of minutes.

As a correction to the evaporation overestimation, an evaporation limiter is included when q_l exceeds 1 g kg^{-1}. The evaporation limiter can be derived by considering the change in mass of a raindrop falling freely through the air, which is governed by the equation

$$\frac{1}{m}\frac{dm}{dt} = -\frac{3c_v D\Delta\rho_v}{a^2\rho_w}, \tag{A3}$$

where m is the mass of the droplet, c_v is a macroscopic diffusion coefficient, D is a microscopic diffusion coefficient, $\Delta\rho_v$ is the change in water vapor density from the surface of the drop to the surrounding environment, a is the radius of the drop, and ρ_w is the density of liquid water (Kinzer and Gunn 1951). By assuming a homogeneous number of drops per unit volume and constant dry density of the local environment during the evaporation process, m can be replaced by q_l. Moreover, if one assumes that the rhs of (A3) is constant, then its inverse represents an e-folding time scale for the change in q_l due to evaporation:

$$\tau_{\text{evap}} = \frac{a^2\rho_w}{3c_v D\Delta\rho_v}. \tag{A4}$$

The parameters in (A4) are empirically estimated in Table 1 herein and Table 2 of Kinzer and Gunn (1951). Assuming a rain drop diameter of 2.2 mm, corresponding roughly to a terminal velocity of -7 m s^{-1} (Gunn and Kinzer 1949) and a temperature of 20°C, τ_{evap} becomes only a function of the relative humidity, as shown in Fig. A1 by the crosses. The evaporation time scale increases with relative humidity, especially as the environment approaches saturation. For a relative humidity of 10%, the time scale is about 6 minutes and increases to about an hour when the relative humidity is 90%.

Since the data from Kinzer and Gunn (1951) is discrete, it is fitted to a tangent curve, as shown by the line in Fig. A1, with the equation of the tangent curve:

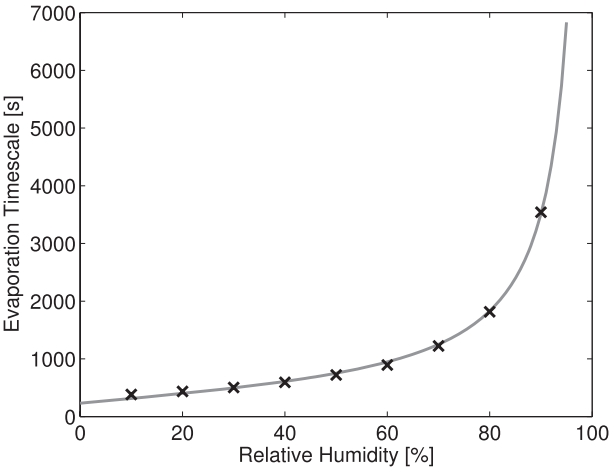

FIG. A1. The evaporation time scale τ_{evap} as a function of the relative humidity. The time scale is derived from Kinzer and Gunn (1951) data for a drop diameter of 22 mm and a temperature of 20°C (crosses). The least squares tangent curve fit to the data is given by the line.

$$\hat{\tau}_{\text{evap}} = 519.59\tan\left(\frac{\pi H}{2}\right) + 231.83. \tag{A5}$$

b. Turbulence

TCs contain a full spectrum of nonaxisymmetric phenomena that an axisymmetric model cannot represent. Consequently, their effects must be parameterized. The turbulence parameterization follows the RE87 parameterization closely, but must be adjusted so that saturated mixing conserves s_p. Moreover, the dry, compressible equations are used instead of the incompressible equations to formulate the turbulence parameterization. This allows the resulting turbulence terms to fit in more neatly with the model's numerical scheme. The resulting turbulent terms in (1)–(7) are

$$D_U = \frac{1}{r}\frac{\partial r\tau_{rr}}{\partial r} + \frac{\partial \tau_{rz}}{\partial z} - \frac{\tau_{\phi\phi}}{r}, \tag{A6}$$

$$D_V = \frac{1}{r^2}\frac{\partial r^2\tau_{r\phi}}{\partial r} + \frac{\partial \tau_{\phi z}}{\partial z}, \tag{A7}$$

$$D_W = \frac{1}{r}\frac{\partial r\tau_{rz}}{\partial r} + \frac{\partial \tau_{zz}}{\partial z}, \tag{A8}$$

$$D_X = -\frac{1}{r}\frac{\partial rF_r^x}{\partial r} - \frac{\partial F_z^x}{\partial z}, \tag{A9}$$

where $X \in \{S_p, \rho_v, \rho_l\}$ and $x \in \{s_p, q_v, q_l\}$. The components of the stress tensor are

$$\begin{pmatrix} \tau_{rr} & \tau_{r\phi} & \tau_{rz} \\ & \tau_{\phi\phi} & \tau_{\phi z} \\ & & \tau_{zz} \end{pmatrix} = \begin{bmatrix} 2\mu_h\left(\frac{\partial u}{\partial r} - \frac{1}{3}\nabla\cdot\mathbf{u}\right) & \mu_h r\frac{\partial}{\partial r}\left(\frac{v}{r}\right) & \mu\left(\frac{\partial u}{\partial z} + \frac{\partial w}{\partial r}\right) \\ & 2\mu_h\left(\frac{u}{r} - \frac{1}{3}\nabla\cdot\mathbf{u}\right) & \mu\left(\frac{\partial v}{\partial z}\right) \\ & & 2\mu\left(\frac{\partial w}{\partial z} - \frac{1}{3}\nabla\cdot\mathbf{u}\right) \end{bmatrix}, \tag{A10}$$

where only the upper right part of the tensor is shown because it is symmetric. These equations are similar to those used in the RE87 and Bryan and Rotunno (2009b) models, with the exception of the added divergence in the diagonal terms of the stress tensor and the replacement of the kinematic viscosity with the dynamic viscosity μ. The turbulent fluxes of the remaining scalar variables are

$$(F_r^x, F_z^x) = -\left(\mu_h\frac{\partial x}{\partial r}, \mu\frac{\partial x}{\partial z}\right). \tag{A11}$$

The dynamic viscosity and its horizontal counterpart, μ_h, are given by

$$\mu = \rho_d l^2 \sigma\sqrt{1 - \mathrm{Ri}}, \tag{A12}$$

$$\mu_h = \rho_d l_h^2 \sigma_h, \tag{A13}$$

where l is the eddy mixing length, l_h is the horizontal eddy mixing length, σ is the deformation, σ_h is the horizontal deformation, and Ri is the flux Richardson number. If $\mathrm{Ri} > 1$, then the flow is dynamically stable and μ is set to zero. For locations where μ exceeds μ_h, μ_h is set to the value of μ such that the mixing is isotropic. Based on the findings of Bryan and Rotunno (2009b), l is set to 100 m and l_h is set to 1500 m. These eddy mixing length scales seem to yield reasonable representations of the intensity evolution in the current model. In the eyewall at the top of the boundary layer, μ_h can approach 10^4 kg m^{-1} s^{-1} for an intense storm.

At the lower boundary the tangential stress and turbulent fluxes are given by the bulk aerodynamic formulas:

$$\tau_{rz}(z = 0) = C_D\rho_d u\sqrt{u^2 + v^2}, \tag{A14}$$

$$\tau_{r\phi}(z = 0) = C_D\rho_d v\sqrt{u^2 + v^2}, \tag{A15}$$

$$F_z^{s_p}(z = 0) = C_k\rho_d\sqrt{u^2 + v^2}(s_p^*|_{\mathrm{SST}} - s_p), \tag{A16}$$

$$F_z^{q_v}(z = 0) = C_k\rho_d\sqrt{u^2 + v^2}(q_v^*|_{\mathrm{SST}} - q_v), \tag{A17}$$

where C_D is the drag coefficient and C_k is the enthalpy exchange coefficient. The saturation pseudoadiabatic entropy s_p^* and the saturation water vapor mixing ratio are evaluated at the sea surface temperature, while all other variables are evaluated at the lowest model level. Here C_D is given by a modified Deacon's formula:

$$C_D = \mathrm{MIN}(1.1\times10^{-3} + 4\times10^{-5}\sqrt{u^2 + v^2}, 3.0\times10^{-3}), \tag{A18}$$

which assumes a linear increase in C_D with wind speed: C_D is capped at a maximum value of 3.0×10^{-3}, which is a simple way of taking into account that C_D does not increase unbounded at high wind speeds (Powell et al. 2003). The value of the cap is chosen to be quite high given uncertainties in the exact values of C_D at high wind speeds.

Additionally, there are large uncertainties with regards to the value of C_k, especially relative to C_D at high wind speeds (Edson et al. 2007; Black et al. 2007). For the purposes of this study, C_k is set equal to C_D to prevent the introduction of an additional degree of freedom that would make it harder to interpret the results.

Following Bister and Emanuel (1998), dissipative heating caused by turbulent dissipation of kinetic energy is added to the model. Dissipative heating in the surface layer recycles heat into the warm reservoir of the TC heat engine, leading to an increase in wind speed and a decrease in pressure. Zhang and Altshuler (1999) and Jin et al. (2007) also found that the heating caused by internal dissipation of turbulent kinetic energy is important for TC intensity.

c. Radiation

Radiation is a part of a TC's idealized thermodynamic cycle and generally represents a sink of entropy. Radiative cooling balances adiabatic warming caused by subsidence associated with the secondary circulation and also helps maintain a reservoir of available potential energy to power the TC. Following RE87, the radiation is prescribed through Newtonian cooling back to the initial, far-field potential temperature profile. The relaxation time scale is chosen to be 12 h, which is the same value used in RE87. To prevent excessive cooling of the TC's warm core, the cooling is capped at 2 K day^{-1},

which is an approximate upper bound on the radiative cooling in clear-sky conditions in the tropics (Hartmann et al. 2001). The effect of clouds and water vapor on the radiation budget is not considered.

REFERENCES

Arakawa, A., and V. Lamb, 1977: Computational design of the basic dynamical process of the UCLA general circulation model. *Methods in Computational Physics,* Vol. 17, J. Chang, Ed., Academic Press, 173–265.

Bister, M., and K. Emanuel, 1998: Dissipative heating and hurricane intensity. *Meteor. Atmos. Phys.,* **65,** 233–240.

Black, P., and Coauthors, 2007: Air-sea exchange in hurricanes: Synthesis of observations from the Coupled Boundary Layer Air–Sea Transfer experiment. *Bull. Amer. Meteor. Soc.,* **88,** 357–374.

Bolton, D., 1980: The computation of equivalent potential temperature. *Mon. Wea. Rev.,* **108,** 1046–1053.

Bryan, G., 2008: On the computation of pseudoadiabatic entropy and equivalent potential temperature. *Mon. Wea. Rev.,* **136,** 5239–5245.

——, and J. Fritsch, 2004: A reevaluation of ice–liquid water potential temperature. *Mon. Wea. Rev.,* **132,** 2421–2431.

——, and R. Rotunno, 2009a: Evaluation of an analytical model for the maximum intensity of tropical cyclones. *J. Atmos. Sci.,* **66,** 3042–3060.

——, and ——, 2009b: The maximum intensity of tropical cyclones in axisymmetric numerical model simulations. *Mon. Wea. Rev.,* **137,** 1770–1789.

Chen, Y., G. Brunet, and M. Yau, 2003: Spiral bands in a simulated hurricane. Part II: Wave activity diagnostics. *J. Atmos. Sci.,* **60,** 1239–1256.

Corbosiero, K., J. Molinari, A. Aiyyer, and M. Black, 2006: The structure and evolution of Hurricane Elena (1985). Part II: Convective asymmetries and evidence for vortex Rossby waves. *Mon. Wea. Rev.,* **134,** 3073–3091.

Cram, T., J. Persing, M. Montgomery, and S. Braun, 2007: A Lagrangian trajectory view on transport and mixing processes between the eye, eyewall, and environment using a high-resolution simulation of Hurricane Bonnie (1998). *J. Atmos. Sci.,* **64,** 1835–1856.

Davies-Jones, R., 2009: On formulas for equivalent potential temperature. *Mon. Wea. Rev.,* **137,** 3137–3148.

Durran, D., 1999: *Numerical Methods for Wave Equations in Geophysical Fluid Dynamics.* Springer, 465 pp.

Edson, J., and Coauthors, 2007: The Coupled Boundary Layers and Air–Sea Transfer experiment in low winds. *Bull. Amer. Meteor. Soc.,* **88,** 341–356.

Emanuel, K., 1986: An air–sea interaction theory for tropical cyclones. Part I: Steady-state maintenance. *J. Atmos. Sci.,* **43,** 585–604.

——, 1994: *Atmospheric Convection.* Oxford University Press, 580 pp.

——, 2004: Tropical cyclone energetics and structure. *Atmospheric Turbulence and Mesoscale Meteorology*, E. Fedorovich, R. Rotunno, and B. Stevens, Eds., Cambridge University Press, 165–192.

Frank, W., and E. Ritchie, 2001: Effects of vertical wind shear on the intensity and structure of numerically simulated hurricanes. *Mon. Wea. Rev.,* **129,** 2249–2269.

Goody, R., 2003: On the mechanical efficiency of deep, tropical convection. *J. Atmos. Sci.,* **60,** 2827–2832.

Gunn, R., and G. Kinzer, 1949: The terminal velocity of fall for water droplets in stagnant air. *J. Meteor.,* **6,** 243–248.

Hartmann, D., J. Holton, and Q. Fu, 2001: The heat balance of the tropical tropopause, cirrus, and stratospheric dehydration. *Geophys. Res. Lett.,* **28,** 1969–1972.

Hendricks, E., and W. Schubert, 2009: Transport and mixing in idealized barotropic hurricane-like vortices. *Quart. J. Roy. Meteor. Soc.,* **135,** 1456–1470.

Holloway, C., and J. Neelin, 2007: The convective cold top and quasi equilibrium. *J. Atmos. Sci.,* **64,** 1467–1487.

Jin, Y., W. Thompson, S. Wang, and C. Liou, 2007: A numerical study of the effect of dissipative heating on tropical cyclone intensity. *Wea. Forecasting,* **22,** 950–966.

Jordan, C., 1958: Mean soundings for the West Indies area. *J. Meteor.,* **15,** 91–97.

Kinzer, G., and R. Gunn, 1951: The evaporation, temperature and thermal relaxation-time of freely falling waterdrops. *J. Meteor.,* **8,** 71–83.

Klemp, J., and R. Wilhelmson, 1978: The simulation of three-dimensional convective storm dynamics. *J. Atmos. Sci.,* **35,** 1070–1096.

——, W. Skamarock, and J. Dudhia, 2007: Conservative split-explicit time integration methods for the compressible nonhydrostatic equations. *Mon. Wea. Rev.,* **135,** 2897–2913.

——, J. Dudhia, and A. Hassiotis, 2008: An upper gravity-wave absorbing layer for NWP applications. *Mon. Wea. Rev.,* **136,** 3987–4004.

Kwon, Y., and W. Frank, 2005: Dynamic instabilities of simulated hurricane-like vortices and their impacts on the core structure of hurricanes. Part I: Dry experiments. *J. Atmos. Sci.,* **62,** 3955–3973.

——, and ——, 2008: Dynamic instabilities of simulated hurricane-like vortices and their impacts on the core structure of hurricanes. Part II: Moist experiments. *J. Atmos. Sci.,* **65,** 106–122.

LeVeque, R., 2002: *Finite-Volume Methods for Hyperbolic Problems.* Cambridge University Press, 558 pp.

Lipps, F., and R. Hemler, 1980: Another look at the thermodynamic equation for deep convection. *Mon. Wea. Rev.,* **108,** 78–84.

McIntyre, M., 1989: On the Antarctic ozone hole. *J. Atmos. Terr. Phys.,* **51,** 29–43.

Möller, J., and M. Montgomery, 1999: Vortex Rossby waves and hurricane intensification in a barotropic model. *J. Atmos. Sci.,* **56,** 1674–1687.

——, and ——, 2000: Tropical cyclone evolution via potential vorticity anomalies in a three-dimensional balance model. *J. Atmos. Sci.,* **57,** 3366–3387.

Montgomery, M., and R. Kallenbach, 1997: A theory for vortex Rossby-waves and its application to spiral bands and intensity changes in hurricanes. *Quart. J. Roy. Meteor. Soc.,* **123,** 435–465.

Nolan, D., and L. Grasso, 2003: Nonhydrostatic, three-dimensional perturbations to balanced, hurricane-like vortices. Part II: Symmetric response and nonlinear simulations. *J. Atmos. Sci.,* **60,** 2717–2745.

——, Y. Moon, and D. Stern, 2007: Tropical cyclone intensification from asymmetric convection: Energetics and efficiency. *J. Atmos. Sci.,* **64,** 3377–3405.

Ooyama, K., 1990: A thermodynamic foundation for modeling the moist atmosphere. *J. Atmos. Sci.,* **47,** 2580–2593.

——, 2001: A dynamic and thermodynamic foundation for modeling the moist atmosphere with parameterized microphysics. *J. Atmos. Sci.,* **58,** 2073–2102.

Pauluis, O., 2007: Sources and sinks of available potential energy in a moist atmosphere. *J. Atmos. Sci.,* **64,** 2627–2641.

——, and I. Held, 2002: Entropy budget of an atmosphere in radiative–convective equilibrium. Part I: Maximum work and frictional dissipation. *J. Atmos. Sci.,* **59,** 125–139.

Powell, M., 1990: Boundary layer structure and dynamics in outer hurricane rainbands. Part II: Downdraft modification and mixed layer recovery. *Mon. Wea. Rev.,* **118,** 918–938.

——, P. Vickery, and T. Reinhold, 2003: Reduced drag coefficient for high wind speeds in tropical cyclones. *Nature,* **422,** 279–283.

Reasor, P., and M. Montgomery, 2001: Three-dimensional alignment and corotation of weak, TC-like vortices via linear vortex Rossby waves. *J. Atmos. Sci.,* **58,** 2306–2330.

——, ——, F. Marks, and J. Gamache, 2000: Low-wavenumber structure and evolution of the hurricane inner core observed by airborne dual-Doppler radar. *Mon. Wea. Rev.,* **128,** 1653–1680.

——, ——, and L. Grasso, 2004: A new look at the problem of tropical cyclones in vertical shear flow: Vortex resiliency. *J. Atmos. Sci.,* **61,** 3–22.

Riemer, M., and M. Montgomery, 2011: Simple kinematic models for the environmental interaction of tropical cyclones in vertical wind shear. *Atmos. Chem. Phys.,* **11,** 9395–9414.

——, ——, and M. Nicholls, 2010: A new paradigm for intensity modification of tropical cyclones: Thermodynamic impact of vertical wind shear on the inflow layer. *Atmos. Chem. Phys.,* **10,** 3163–3188.

Rotunno, R., and K. Emanuel, 1987: An air–sea interaction theory for tropical cyclones. Part II: Evolutionary study using a nonhydrostatic axisymmetric numerical model. *J. Atmos. Sci.,* **44,** 542–561.

Rutherford, B., G. Dangelmayr, J. Persing, M. Kirby, and M. Montgomery, 2010a: Lagrangian mixing in an axisymmetric hurricane model. *Atmos. Chem. Phys.,* **10,** 6777–6791.

——, ——, ——, W. Schubert, and M. Montgomery, 2010b: Advective mixing in a nondivergent barotropic hurricane model. *Atmos. Chem. Phys.,* **10,** 475–497.

Sapsis, T., and G. Haller, 2009: Inertial particle dynamics in a hurricane. *J. Atmos. Sci.,* **66,** 2481–2492.

Schecter, D., M. Montgomery, and P. Reasor, 2002: A theory for the vertical alignment of a quasigeostrophic vortex. *J. Atmos. Sci.,* **59,** 150–168.

Schubert, W., M. Montgomery, R. Taft, T. Guinn, S. Fulton, J. Kossin, and J. Edwards, 1999: Polygonal eyewalls, asymmetric eye contraction, and potential vorticity mixing in hurricanes. *J. Atmos. Sci.,* **56,** 1197–1223.

Simpson, R., and R. Riehl, 1958: Mid-tropospheric ventilation as a constraint on hurricane development and maintenance. Preprints, *Tech. Conf. on Hurricanes,* Miami Beach, FL, Amer. Meteor. Soc., D4-1–D4-10.

Smith, R., 2006: Accurate determination of a balanced axisymmetric vortex in a compressible atmosphere. *Tellus,* **58A,** 98–103.

Srivastava, R., 1987: A model of intense downdrafts driven by the melting and evaporation of precipitation. *J. Atmos. Sci.,* **44,** 1752–1774.

Tang, B., and K. Emanuel, 2010: Midlevel ventilation's constraint on tropical cyclone intensity. *J. Atmos. Sci.,* **67,** 1817–1830.

Tripoli, G., and W. Cotton, 1981: The use of ice-liquid water potential temperature as a thermodynamic variable in deep atmospheric models. *Mon. Wea. Rev.,* **109,** 1094–1102.

Wang, Y., 2002: Vortex Rossby waves in a numerically simulated tropical cyclone. Part I: Overall structure, potential vorticity, and kinetic energy budgets. *J. Atmos. Sci.,* **59,** 1213–1238.

Wicker, L., and W. Skamarock, 2002: Time-splitting methods for elastic models using forward time schemes. *Mon. Wea. Rev.,* **130,** 2088–2097.

Zeng, X., W. Tao, and J. Simpson, 2005: An equation for moist entropy in a precipitating and icy atmosphere. *J. Atmos. Sci.,* **62,** 4293–4309.

Zhang, D., and E. Altshuler, 1999: The effects of dissipative heating on hurricane intensity. *Mon. Wea. Rev.,* **127,** 3032–3038.